KeAi
CHINESE ROOTS
GLOBAL IMPACT

Available online at www.keaipublishing.com/en/journals/journal-of-magnesium-and-alloys/

ScienceDirect

Journal of Magnesium and Alloys 13 (2025) 3702–3712

www.elsevier.com/locate/jma

Full Length Article

# Formation mechanism of cluster-arranged layers in Mg-Y-Zn alloy: A density functional theory study ☆

Ryosuke Matsumoto*, Naoki Uemura

*Department of Mechanical and Electrical Systems Engineering, Kyoto University of Advanced Science, 18, Yamanouchi-Gotandacho, Ukyo-ward, Kyoto 615-8577, Japan*

Received 9 April 2025; received in revised form 17 June 2025; accepted 9 July 2025
Available online 12 August 2025

**Abstract**

A sparsely introduced basal intrinsic 2-type stacking fault ($I_2$-SF) with a dense segregation of clusters (cluster-arranged layer; CAL) in $\alpha$-Mg exerts a sufficient strengthening effect with a reduced content of additive elements. Moreover, the dynamic nucleation and growth of CALs during deformation largely improves the creep resistance. This paper analyzes the cosegregation behaviors of yttrium (Y) and zinc (Zn) atoms at an $I_2$-SF in bulk and at basal edge dislocations using density functional theory calculations. We also study the modification of the generalized stacking-fault energy (GSFE) curves associated with the cosegregation. The segregation energies of Y and Zn atoms in the $I_2$-SF are relatively small during the initial segregation of a cluster, but increases stepwise as the cluster grows. After introducing Y and Zn atoms in the $I_2$-SF in an energetically stable order, we obtain an $L1_2$-type cluster resembling that reported in the literature. Small structural changes driven by vacancy diffusion produce an exact $L1_2$-type cluster. Meanwhile, the core of the Shockley partial dislocation generates sufficient segregation energy for cluster nucleation. Migration of the Shockley partial dislocation and expansion of the $I_2$-SF part are observed at a specific cluster size. The migration is triggered by a large modification of the GSFE curve and destabilization of the hexagonal close-packed stacking (hcp) by the segregated atoms. At this point, the cluster has reached sufficient size and continues to follow the growth in the $I_2$-SF part. According to our findings, the CAL at elevated temperature is formed through repeated synchronized behavior of cluster nucleation at the Shockley partial dislocation, dislocation migration triggered by the destabilized hcp stacking, and following of cluster growth in the $I_2$-SF part of the dislocation.


*Keywords:* Generalized stacking-fault energy; Basal dislocation, Segregation; Density functional theory; Long-period stacking-ordered phase; Cluster-arranged layer.

## 1. Introduction

Owing to their excellent strength-to-weight ratios, magnesium (Mg) and its alloys have been extensively studied, and their use is expected to expand in various engineering fields, especially in the transportation fields [1]. However, as a structural material, the advantage of Mg to other lightweight metals and alloys, especially with high-strength aluminum alloys, is insufficient. Sophisticated control of the microstructure with various phases and regions of different grain sizes, textures, or defect concentrations is considered to enhance the mechanical properties of Mg-alloys.

One unique and promising phase found in Mg-alloys is the long-period stacking-ordered (LPSO) phase, which possesses a synchronized stacking-and-segregation structure. An LPSO-phase Mg alloy, first developed by Kawamura et al. through rapidly solidified powder metallurgy, exhibits notably high strength and ductility [2]. Additive elements, typically zinc (Zn) and yttrium (Y), form $L1_2$-type clusters in periodically introduced intrinsic 2-type stacking faults ($I_2$-SFs) [3–5]. The detailed formation mechanisms of the LPSO phase

*Abbreviations:* CAL, Cluster-arranged layer; fcc, Face-centered cubic; GSFE, generalized stacking-fault energy; hcp, Hexagonal close packing; $I_1$-SF, intrinsic 1-type stacking fault; $I_2$-SF, intrinsic 2-type stacking fault; LPSO, long-period stacking ordered; SF, Stacking fault.

☆ Peer review under the responsibility of Chongqing University.

* Corresponding author.
*E-mail address:* matsumoto.ryosuke@kuas.ac.jp (R. Matsumoto).

https://doi.org/10.1016/j.jma.2025.07.013

and cluster structures have been analyzed through atomistic simulations [6], density functional theory (DFT) calculations [7], and experimental observations [8]. The LPSO phase effectively improves the strengths of bimodal and multimodal Mg-alloys [9–13]. However, the LPSO phase requires relatively high contents of expensive additives such as Y and late lanthanide elements (Gd, Tb, Dy, Ho, Er, and Tm) [14].

Sparsely formed stacking faults (SFs) with dense segregation of clusters, which correspond to a single $I_2$-SF in the LPSO phase, have been recently identified in $\alpha$-Mg in dilute alloy systems. These sparsely introduced structures, called cluster-arranged layers (CALs), provide sufficient strengthening with reduced amounts of expensive additive elements [15–17]. He et al. [18] reported the dense bismuth (Bi) segregation at the intrinsic 1-type SF ($I_1$-SF) in the $\alpha$-Mg phase of Mg–Bi alloys and discussed the strengthening effect by the segregation. Mineta et al. [19] reported the dynamic formation of CALs (called *plate-like LPSOs* in their paper) in recrystallized $\alpha$-Mg during a creep test of annealed multimodal Mg–Y–Zn alloy. They also reported the enhanced formation of CALs in alloys annealed at higher temperatures, especially at 793 K, along with increased creep resistance accompanied by kink-band formation. Although Mineta et al. predicted that CALs form through basal dislocation motions, the detailed mechanisms must be clarified for effectively introducing CALs as strengthening agents in dilute Mg-alloys.

Microscopic phenomena can be effectively analyzed through large-scale spatiotemporal atomistic simulations [20,21]. However, the analyses of multi-element systems are restricted by the limitations in the interatomic potentials. Implementing large-scale DFT calculations, we investigate the cosegregation behaviors of Y and Zn atoms at an $I_2$-SF in bulk and in basal edge dislocations consisting of two Shockley partial dislocations and an $I_2$-SF part. We also evaluate the modification of the generalized stacking-fault energy (GSFE) curves caused by cluster segregation. Integrating these results, we clarify that CAL formation is driven by the synchronized behaviors of the dislocation motions and cosegregation.

## 2. Analysis method

### 2.1. Density functional theory

DFT calculations were performed using the Vienna Ab initio Simulation Package [22]. We employed the projector augmented-wave method with the Perdew–Burke–Ernzerhof generalized gradient approximation as the exchange-correlation function [23,24], and the Monkhorst–Pack scheme [25] for k-point sampling. The number of k-points in each calculation is stated in Subsections 2.2 and 2.4. The cutoff energy was set to 360 eV. All simulations were performed in a supercell with periodic boundary conditions in all directions. The atomic positions were fully relaxed under a force tolerance of 0.01 eV/Å unless otherwise stated. These settings are based on previous studies [26,27]. To ensure a stress of 2 MPa at the most at the initial state, we removed the normal stress along each axis by updating the cell size and maintaining fixed angles between the cell vectors. However, if a large SF plane (or long straight dislocation) is isolated in a bulk hexagonal close-packed (hcp) structure, the expansion or shrinkage along the directions parallel to the SF (or dislocation line) is constrained by the surrounding lattice. To account for this scenario, the cell size was not relaxed in the SF model doped with Y and Zn atoms (Subsection 2.2) or in the dislocation models (Subsection 2.4).

### 2.2. Cosegregation behavior at the stacking fault

To analyze the cosegregation behavior of the Y and Zn atoms at the $I_2$-SF, we sequentially substituted a Y or Zn atom in the most energetically stable order. The simulation models and evaluation procedures are described below.

1) In the bulk-hcp model (Fig. 1a), 48 Mg atoms were arranged in four atomic layers along [0001] (12 atoms per layer). In the SF model (Fig. 1b), 216 Mg atoms were arranged in 18 atomic layers along [0001] (12 atoms per layer). The *x*-, *y*-, and *z*-axes in both models were set parallel to $[10\bar{1}0]$, $[\bar{1}2\bar{1}0]$, and [0001], respectively. The slab (or film) with an $I_2$-SF was isolated by an approximately 2.3-nm thick vacuum layer (Fig. 1b; note that the periodic boundary condition was applied in all directions). The $I_2$-SF, which comprises two face-centered cubic (fcc) stacking layers [28], was located at the center of the slab. Fig. 1c shows the atomic positions in the A, B, and C-stacking layers. DFT calculations of the bulk-hcp and SF models were performed on $5 \times 5 \times 7$ and $5 \times 5 \times 1$ k-point meshes, respectively. After relaxation, the energies of the bulk-hcp and SF models were $E_{\mathrm{hcp}} = -72.30$ eV and $E_{\mathrm{SF}_0} = -317.87$ eV, respectively.

2) The atomic positions and cell lengths were fully relaxed after replacing one Mg atom in the bulk-hcp model by a Y or Zn atom. The energies of the bulk-hcp with one Y and one Zn atom ($E^x_{\mathrm{hcp}}$; $x$ = Y or Zn) were then calculated as $E^{\mathrm{Y}}_{\mathrm{hcp}} = -77.29$ eV and $E^{\mathrm{Zn}}_{\mathrm{hcp}} = -71.93$ eV, respectively.

3) Similar to step 2), the energy of the SF model with one Y or Zn was calculated around the $I_2$-SF. As this energy depends on the position of the substitution atom, the substitution site was varied among the middle eight layers (two fcc layers, the upper three hcp layers, and the lower three hcp layers) (Fig. 1b). The segregation energy ($\Delta E^{x_i}_{\mathrm{seg}_1}$), which is equivalent to the trapping energy [29], was calculated as

$$\Delta E^{x_i}_{\mathrm{seg}_1} = -\left\{\left(E^{x_i}_{\mathrm{SF}_0} + E_{\mathrm{hcp}}\right) - \left(E_{\mathrm{SF}_0} + E^{x}_{\mathrm{hcp}}\right)\right\}, \quad (1)$$

where $E^{x_i}_{\mathrm{SF}_0}$ is the energy of the SF model with element $x$ at site $i$. If $E^{x_i}_{\mathrm{SF}_0}$ is large and positive, element $x$ is strongly bound to the SF. Finally, the segregation site, segregation element, and segregation energy ($\Delta E_{\mathrm{seg}_1}$) of the first segregation were determined from the structure with the largest segregation energy, i.e., $\Delta E_{\mathrm{seg}_1} = \max(\Delta E^{x_i}_{\mathrm{seg}_1})$. The energy of the SF model after the first segregation is denoted by $E_{\mathrm{SF}_1}$.

4) By repeating step 3) for each of 13 substitution atoms, the most stable site $i$ and element $x$ were determined at each segregation. The segregation energy ($\Delta E^{x_i}_{\mathrm{seg}_n}$) of the $n$th seg-

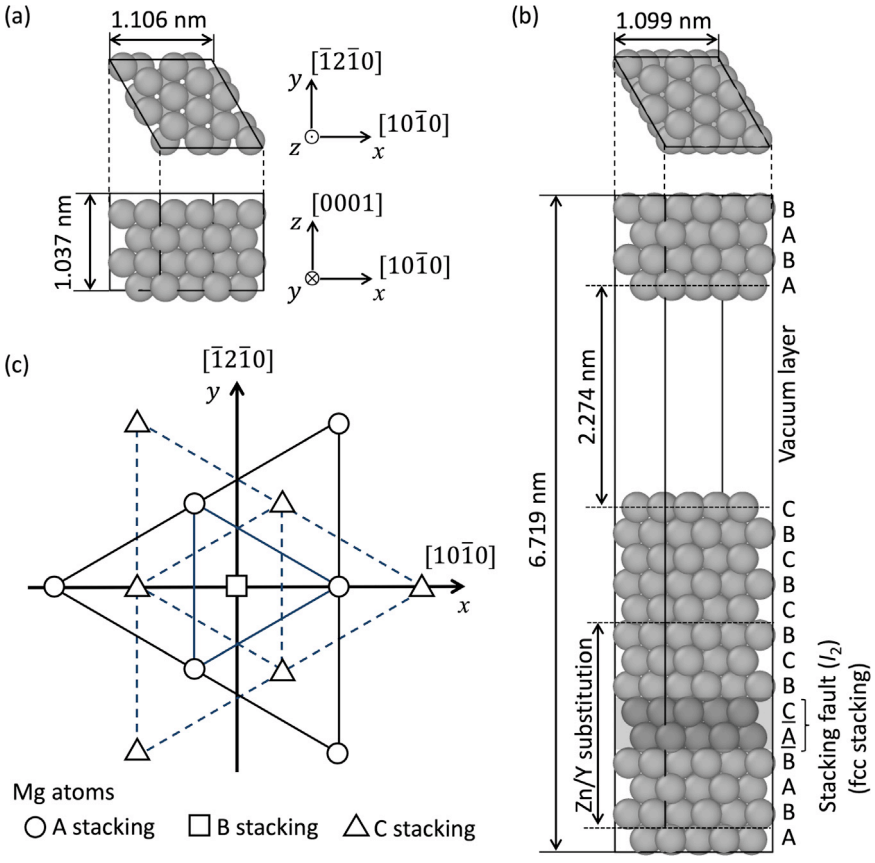


Fig. 1. Atomic structures used in the cosegregation behavior analysis of Y and Zn at the intrinsic 2-type stacking fault ($I_2$-SF) in Mg: (a) bulk-hcp model and (b) SF model with an $I_2$-SF; (c) atomic positions in the A, B, and C-stacking layers shown in (b).

regation of element $x$ at site $i$ was calculated as

$$\Delta E^{x_i}_{\mathrm{seg}_n} = -\left\{\left(E^{x_i}_{\mathrm{SF}_{n-1}} + E_{\mathrm{hcp}}\right) - \left(E_{\mathrm{SF}_{n-1}} + E^{x}_{\mathrm{hcp}}\right)\right\}. \quad (2)$$

The site $i$, element $x$, $\Delta E_{\mathrm{seg}_n}$, and $E_{\mathrm{SF}_n}$ of the $n$th segregation were determined similarly to those of the first segregation. During actual segregation, the order and position can be modified by the thermal effect [29]. However, direct treatment using a statistical mechanics-based method, such as Monte Carlo [6], infeasibly increases the calculation cost of DFT or requires the development of reliable interatomic potentials. We believe that the proposed method simulates statistically plausible segregation behavior.

The occupancy of the $n$th segregation was estimated using the following Langmuir–McLean equation [30]:

$$\frac{c_n}{(1-c_n)} = \frac{c^x_{\mathrm{hcp}}}{1-c^x_{\mathrm{hcp}}} \exp\left(\frac{\Delta E_{\mathrm{seg_n}}}{k_{\mathrm{B}}T}\right), \quad (3)$$

where $c^x_{\mathrm{hcp}}$ is the atomic fraction of element $x$ assumed in the bulk-hcp phase, $x$ denotes Y or Zn, which segregates during the $n$th segregation, and $k_{\mathrm{B}}$ and $T$ are the Boltzmann's constant and temperature, respectively. Based on Ref [19], we assumed $c^{\mathrm{Y}}_{\mathrm{hcp}} = 1.8$ at.%, $c^{\mathrm{Zn}}_{\mathrm{hcp}} = 0.5$ at.%, and $T = 523$ K. The concentrations correspond to the solute concentrations in the recrystallized region after heat treatment at 793 K, at which the concentration was maximized and the CAL formation was most effective during the creep test at 523 K. As explained in Steps 3) and 4), the segregation position and element were determined by the segregation energy, not by the occupancy given by Eq. (3), which depends on the solute concentration. Deciding the element at each segregation in terms of occupancy will minimally alter the obtained results at the concentration difference between the Y and Zn atoms in the present study.

### 2.3. Calculation of generalized stacking-fault energy

The slip plane was set at the mid-plane of the SF (between the A and C layers in Fig. 1b). The upper part of the slab (9 atomic layers) was rigidly displaced along [$10\bar{1}0$] (the $x$-axis) by $\Delta x = j \times (b_{\mathrm{partial}}/20)$ where $j = 0, 1, 2, \cdots, 20$, and $b_{\mathrm{partial}}$ is the magnitude of the Burgers vector of the Shockley partial dislocation. The atomic structures along the $y$- and $z$-direction were then relaxed under the constraint along the $x$-direction.

The GSFE at displacement $\Delta x$ was calculated as

$$\gamma_{\mathrm{GSFE}_n}(\Delta x) = \frac{E_{\mathrm{SF}_n}(\Delta x) - E_{\mathrm{SF}_n}(0)}{A}, \quad (4)$$

where $E_{\mathrm{SF}_n}(\Delta x)$ is the energy of the slab model with $n$ segregation atoms at displacement $\Delta x$. $A$ denotes the cross-sectional area parallel to the slip plane. Note that the GSFE in this paper is defined for fcc stacking (the $I_2$-SF structure) as a reference structure.

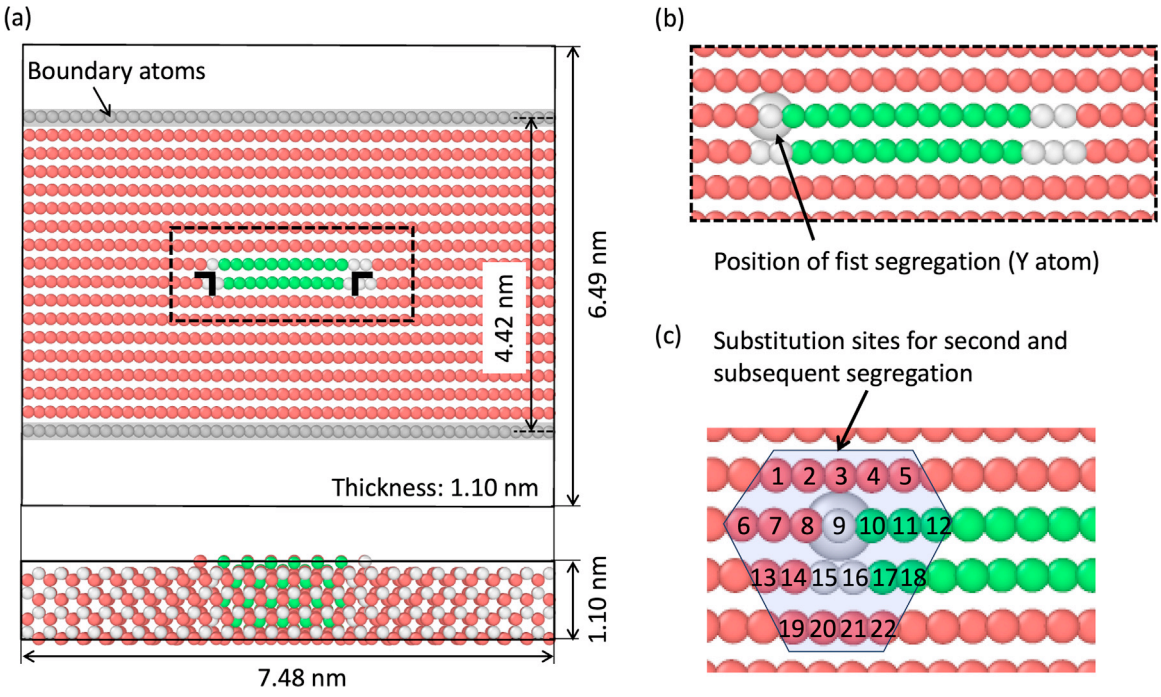


Fig. 2. Atomic structure (thick model) used in the cosegregation behavior analysis of Y and Zn at a basal edge dislocation in Mg. The red, green, blue, and gray dots represent atoms with hcp, fcc, body-centered cubic (bcc), and other local structures, respectively. Panel (a) demonstrates the thick dislocation model, (b) shows the first segregation position of Y, and (c) depicts the insertion positions of the second and subsequent segregation. Positions in the front and back layers are labeled 1–22 and 1′–22′, respectively. The first Y position in (b) corresponds to position 9′ in (c) (color online).

The unstable SF energy associated with the stacking change from fcc ($I_2$-SF) to hcp is defined as

$$\gamma_{\mathrm{USF}_n} = \max\left(\gamma_{\mathrm{GSFE}_n}(\Delta x)\right) - \gamma_{\mathrm{GSFE}_n}(0). \quad (5)$$

During a transition from fcc-to-hcp stacking, the energy changes by $\Delta E_{\mathrm{fcc\_to\_hcp}_n} = \gamma_{\mathrm{GSFE}_n}(b_{\mathrm{partial}}) - \gamma_{\mathrm{GSFE}_n}(0)$. The unstable SF energy associated with the stacking change from the hcp is given by $\gamma_{\mathrm{USF}_n}{}' = \gamma_{\mathrm{USF}_n} - \Delta E_{\mathrm{fcc\_to\_hcp}_n}$.

### 2.4. Segregation behavior at basal dislocation

The segregation behaviors of the Y and Zn atoms near the core of the basal dislocation were analyzed in large atomic models with different thickness. The thin model is expected to be less influenced by boundaries than the thick model, but the substitution atoms are closely arranged along the dislocation line, and $L1_2$-type clusters cannot form because their diameter exceeds the model thickness. Therefore, the thin model was used to determine the segregation position of the first atom in the dislocation core. Subsequent segregations around the first segregation position were then investigated in the thick model.

The details of the thin model and the results are shown in Appendix. The thick model with 1692 Mg atoms (Fig. 2a) was twice as thick as the thin model (1.10 nm along the $z$-axis) but its width and height were reduced to 7.48 nm and 4.42 nm, respectively. A vacuum layer (~2.1 nm) was set above and below the slab. $1 \times 1 \times 5$ k-point meshe was employed for the thick model. An edge dislocation was introduced at the center of the slab, as described in Ref [31–33]. The structures were relaxed under the fixed motion of the boundary atoms (movement of the atoms in the top and bottom layers along the $y$-axis as indicated in Fig. 2a and Fig. A1). The crystal structure was analyzed using common neighbor analysis [34] incorporated in the OVITO-Open Visualization Tool [35]. The basal dislocations in Figs. 2 and A1 exhibit an expanded core structure, in which the two fcc layers corresponding to $I_2$-SF are terminated by two Shockley partial dislocations. The $I_2$-SF is approximately 1.8-nm wide in both models.

Fig. 2b shows the first segregation atom (Y) obtained in Appendix. The selected substitution positions in the thick model (Fig. 2c) were labeled 1 to 22. The two atoms overlapped along the thickness direction. The first segregation atom (Y) existed at position 9′ (see Appendix), where the apostrophe (′) denotes that the atom occupied the behind layer. The segregation energy was calculated similarly to Eqs. (1) and (2) but the energy of the system with an SF ($E^{x_i}_{\mathrm{SF}_{n-1}}$ and $E_{\mathrm{SF}_{n-1}}$) was replaced with the energy of the system with a dislocation ($E^{x_i}_{\mathrm{dis}_{n-1}}$ and $E_{\mathrm{dis}_{n-1}}$).

## 3. Results and discussion

### 3.1. Cosegregation behavior of Y and Zn at $I_2$-SF and formation of an $L1_2$-type cluster

Fig. 3 shows the Y–Zn clusters at $n = 3$, 6, 8, and 13. Segregation was confirmed only in the $I_2$-SF (two fcc layers) and the neighboring hcp layers (immediately above and below the $I_2$-SF). Fig. 4 shows the positional order of the

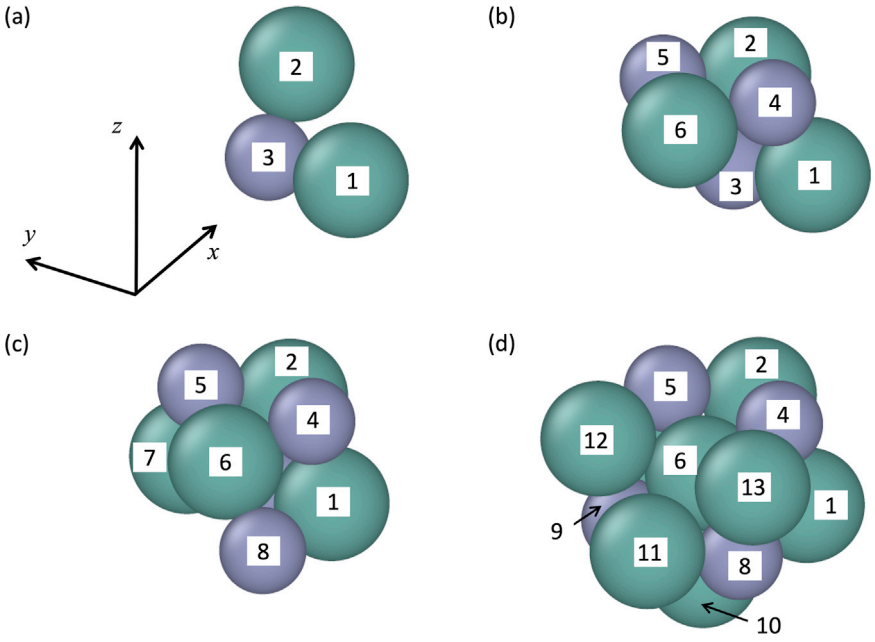


Fig. 3. Y–Zn clusters formed in $I_2$-SF: Structures with (a) $n = 3$, (b) 6, (c) 8, and (d) 13. Y and Zn atoms are represented by large (dark green) and small (dark purple) spheres, respectively (other atoms are not shown). Numbers indicate the order of atomic segregation and correspond to numbers in Fig. 4 (color online).

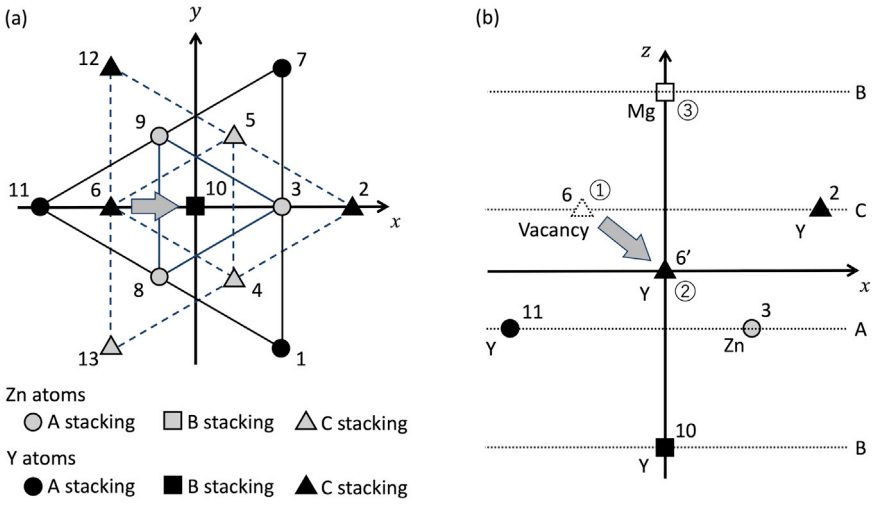


Fig. 4. Positional ordering of Zn and Y around $I_2$-SF until the 13th segregation: positions of Zn and Y projected on (a) the $x$–$y$ plane and (b) $x$–$z$ plane. At sites ①, ②, and ③, different atoms or vacancy occupied compared to the $L1_2$-type cluster. Bold gray arrows in (a) and (b) show atomic migrations during segregation.

segregation, and Table 1 lists the segregation elements $x$, segregation energies $\Delta E_{\mathrm{seg}_n}$, and occupancies $c_n$ during the $n$th segregation.

During the first segregation ($n = 1$), the Y atom possessed the largest segregation energy ($\Delta E_{\mathrm{seg}_1} = 0.05$ eV) in the $I_2$-SF (Table 1). In contrast, the Zn atom negligibly interacted ($\sim 0.1$ eV) with the $I_2$-SF and was not segregated. From these results, Y was identified as the first segregation atom, and its occupancy was calculated as $c_1 = 0.05$ from Eq. (3). Once the Y atom has segregated at the $I_2$-SF, the Zn atom segregates and nucleation of the Y–Zn cluster begins. The segregation energy and occupancy increase stepwise throughout the fol-

Table 1
Segregation elements, segregation energies, and occupancies during the $n$th segregation at $I_2$-SF.

| $n$th segregation | 1 | 2 | 3 | 4 | 5 | 6 | 7 |
|---|---|---|---|---|---|---|---|
| Element $x$ | Y | Y | Zn | Zn | Zn | Y | Y |
| $\Delta E_{\mathrm{seg}_n}$ [eV] | 0.05 | 0.14 | 0.17 | 0.20 | 0.21 | 0.29 | 0.38 |
| $c_n$ (523 K) | 0.05 | 0.30 | 0.17 | 0.28 | 0.34 | 0.91 | 0.99 |
| | 8 | 9 | 10 | 11 | 12 | 13 | |
| | Zn | Zn | Y | Y | Y | Y | |
| | 0.55 | 0.74 | 0.66 | 0.23 | 0.30 | 0.33 | |
| | 1.00 | 1.00 | 1.00 | 0.76 | 0.93 | 0.97 | |

Table 2
Structural changes and energy gains in the structure after the 13th segregation to form the $L1_2$-type cluster with a central Mg atom. Positions at site ①, ②, and ③ are indicated in Fig. 4b, and "Vac" denotes a vacancy.

| | $n = 13$ | (1) | (2) | (3) | (4) | (5) |
|---|---|---|---|---|---|---|
| Site ① | Vac | Mg | Mg | Mg | Vac | Zn |
| Site ② | Y | Y | Y | Vac | Mg | Mg |
| Site ③ | Mg | Mg | Vac | Y | Y | Y |
| Energy gain $\Delta E$ [eV] | – | −0.60 | −0.38 | 1.21 | 1.59 | 0.40 |

lowing segregations, being relatively small ($\leq$ 0.21 eV and $\leq$ 0.34, respectively) for $2 \leq n \leq 5$ and much larger ($\geq$ 0.3 eV and $>$ 0.9, respectively) for $n \geq 6$ except for $n = 11$. The initial cluster growth ($n \leq 5$) is relatively slow because many segregated atoms desorb. Later, cluster growth ($n \geq 6$) is expected to accelerate because the Zn or Y atoms diffusing to the clusters are easily captured and the sites remain occupied with high probability. The initial segregation is markedly enhanced by the dislocation core, as shown in Subsection 3.3.

When the Y and Zn atoms were sequentially introduced, we confirmed that the stable position of the Y atom was usually unstable for the Zn atom and vice versa. Accordingly, a nested structure of Y and Zn atoms resembling an $L1_2$-type cluster was formed (Figs. 3 and 4a). The cluster structure at $n = 13$ differed from the perfect $L1_2$-type cluster reported in the literature [4,5,7]. Specifically, site ① in Fig. 4b was initially occupied by Y at $n = 6$ (Fig. 3b). During the subsequent segregation, the Y atom gradually migrated to the center of the Zn–Y cluster at site ② (gray bold arrows in Fig. 4; see also Fig. 3b–d), leaving a vacancy at site ①, which is occupied by Zn in the $L1_2$-type cluster. The Y atom now occupied the interstitial site at the center ②, which is occupied by Mg in the $L1_2$-type cluster (Fig. 3d). Site ③, which should be occupied by Y, was retained by the Mg atom because the segregation ceased at $n = 13$.

During the 14th substitution, the Y atom was introduced at site ③ with $\Delta E_{\mathrm{seg}_{14}} = 0.42$ eV. However, the formed cluster was $Y_9$–$Zn_5$, requiring the adsorption of a Y atom to form an $L1_2$-type cluster composed of eight Y atoms and six Zn atoms. Here, we considered several structural changes driven by vacancy diffusion to convert the structure at $n = 13$ to the $L1_2$-type cluster and calculated the energies of the intermediate structures. Table 2 presents an energetically and structurally plausible process and the energy difference between the new and existing structures. Throughout this process, 1) the vacancy at site ① is filled with Mg; 2) the vacancy moves to site ③, 3) then to site ② (while the Y atom at site ② moves to site ③), and 4) finally to site ① (while the Mg atom at site ① moves to site ②); finally, 5) a Zn atom arrives at the vacant site ①. The first and second structural changes require additional energies of 0.60 eV and 0.38 eV, respectively, which are easily overcome at elevated temperatures even when considering the activation energy of the necessary vacancy migration (only ~0.4 eV in Mg [36–38]). The latter structural changes confer a large energy benefit, forming an $L1_2$-type cluster with an Mg atom at the central interstitial site. Other processes leading to an $L1_2$-type cluster from the

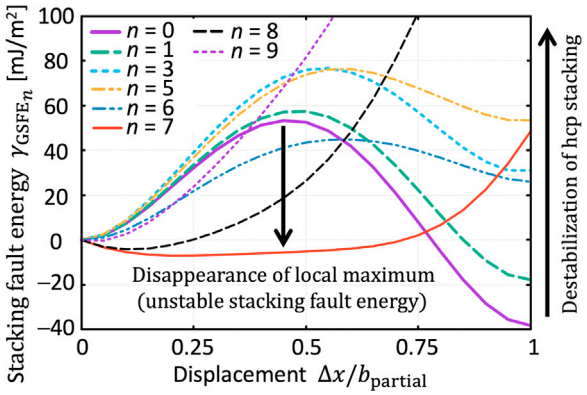


Fig. 5. Generalized stacking-fault energy curves for different numbers of segregation $n$ (color online).

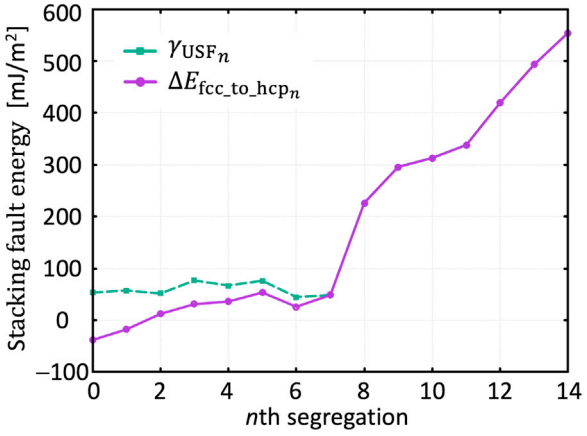


Fig. 6. Unstable stacking-fault energy ($\gamma_{\mathrm{USF}n}$) and energy change associated with transition from face-centered cubic (fcc) stacking to hexagonal closest packing (hcp) stacking ($\Delta E_{\mathrm{fcc\_to\_hcp}_n}$) as a function of number of segregation $n$ (color online).

structure at $n < 13$ are expected. Some such processes may be more energetically favorable than the current process. By simply substituting Y and Zn atoms in a stable order at the $I_2$-SF and implementing atomic exchanges based on vacancy diffusion, we formed an $L1_2$-type cluster. As discussed in Ref [7], any $L1_2$-type cluster with an interstitial atom at the center forms a vacancy, promoting structural change toward a stable structure.

### 3.2. Modification of the generalized stacking-fault energy accompanied by cluster growth

Fig. 5 shows the GSFE curves for different numbers of segregations $n$. The profile of pure Mg ($n = 0$) with $\gamma_{\mathrm{USF}_0'} = 91.4$ mJ/m² and $\Delta E_{\mathrm{fcc\_to\_hcp}_0} = -38.16$ mJ/m² agrees with the literature [27,39,40]. The SF energies in the hcp structure with one Y atom on the slip plane ($n = 1$) ($\gamma_{\mathrm{USF}_1'} = 75.2$ mJ/m² and $\Delta E_{\mathrm{fcc\_to\_hcp}_1} = -17.8$ mJ/m²) are also consistent with the reference values (74.7 mJ/m² and −26.4 mJ/m²[40]). Fig. 6 shows the unstable SF energy ($\gamma_{\mathrm{USF}n}$) and the energy change from fcc-to-hcp stacking ($\Delta E_{\mathrm{fcc\_to\_hcp}_n}$). The unstable SF energy slightly increases at

Table 3
Segregation elements, segregation positions, segregation energies, and occupancies at the $n$th segregation in a Shockley partial dislocation in the thick model.

| $n$th segregation | (1) | 2 | 3 | 4 | 5 | 6 | 7 | 8 | 9 |
|---|---|---|---|---|---|---|---|---|---|
| Element $x$ | (Y) | Zn | Zn | Y | Zn | Y | Zn | Y | Zn |
| Position $i$ | 9′ | 16′ | 15′ | 8′ | 14 | 15 | 13 | 6 | 7 |
| $\Delta E_{\mathrm{seg}_n}$ [eV] | 0.20 | 0.31 | 0.33 | 0.25 | 0.28 | 0.34 | 0.31 | 0.35 | 0.53 |
| $c_n$(523 K) | 0.65 | 0.83 | 0.88 | 0.83 | 0.73 | 0.97 | 0.84 | 0.98 | 1.00 |

the initial segregation ($n = 1$ to 5) but decreases at $n = 6$. Unstable SF energy and hcp stacking energy ($\Delta x/b_{\mathrm{partial}} = 1$) are very similar at $n = 6$ (Fig. 5). At $n = 7$, the energy at the initial local maximum position ($\Delta x/b_{\mathrm{partial}} \sim 0.5$) decreases more than $n = 6$, and the local minimum at hcp stacking ($\Delta x/b_{\mathrm{partial}} = 1$) disappears, markedly changing the shape of the GSFE curve. At $n \geq 7$, $\gamma_{\mathrm{USF}_n}$ and $\Delta E_{\mathrm{fcc\_to\_hcp}_n}$ are equal because the unstable (relative maximum) point in the transition disappears.

The energy change from fcc-to-hcp stacking ($\Delta E_{\mathrm{fcc\_to\_hcp}_n}$) is initially negative, which implies that hcp stacking is more stable than fcc. Thereafter, $\Delta E_{\mathrm{fcc\_to\_hcp}_n}$ monotonically increases except at $n = 6$. At $n = 2$, when the energy change first becomes positive, fcc stacking ($I_2$-SF) is stabilized by a small amount of segregated Y and Zn atoms. The energy difference greatly increases at $n \geq 8$. Once the clusters are formed in the SF, the fcc-to-hcp stacking change becomes quite difficult.

### 3.3. Segregation behavior around the Shockley partial dislocation

Table 3 summarizes the segregation energies evaluated in the thick model and Fig. 7 plots the segregation energies (Fig. 7a) and occupancies of Y and Zn (Fig. 7b) at the $I_2$-SF in the bulk-hcp lattice and dislocation core versus the number of segregated atoms. Fig. 8 shows the atomic structures (Fig. 8a–c) and cluster structures together with the dislocation core structures (Fig. 8d–f) during segregation. The crystal structures were visualized as described for Fig. 2. The slip plane and burgers vector in Fig. 8d–f were analyzed using the dislocation extraction algorithm [41]. The thick model gave the same segregation energy for the first segregation (Y atom at position 9′) as the thin model (namely, 0.20 eV; Table A1). Unlike basal screw dislocation [39], basal edge dislocation did not cause obvious shrinkage of the core structure by Y. During the initial segregation ($n \leq 6$), the segregation energy is higher at the dislocation core than at the $I_2$-SF (Fig. 7a), increasing the occupancy at the dislocation core (Fig. 7b). In contrast, the segregation energy is smaller at the dislocation core than at $I_2$-SF at $n = 7$, 8, and 9. The number of stable positions in the core of the Shockley partial dislocation is probably limited by the disordered structure and the small core size, which hinder the formation of an ordered structure. Table 3 and Fig. 2c confirm a leftward movement of the segregation positions at $n = 7$, 8, and 9. Here, we also confirm a leftward migration of the dislocation core at $n = 9$ (Fig. 8c and 8f).

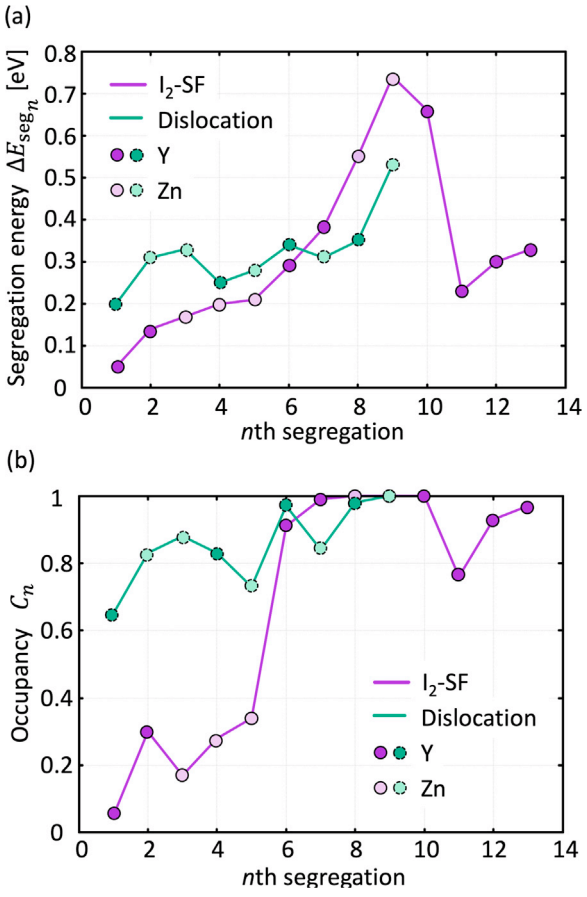


Fig. 7. Comparisons of (a) segregation energy and (b) occupancy at $I_2$-SF in the bulk-hcp lattice and Shockley partial dislocation at different numbers of segregation $n$ (color online).

Fig. 9 schematizes the formation mechanism of a CAL via the synchronization between the segregation of atoms and migration of the Shockley partial dislocation. The material must be maintained within the temperature range that sufficiently activates diffusion of the segregation atoms while retaining a high occupancy of those atoms at the dislocation core (bottom-left panel of Fig. 9). A lower segregation energy reduces occupancy at the same temperature. Although the temperature must then be reduced to allow formation, it delays the atomic diffusion. In contrast, if the segregation energy is higher, the temperature can be raised to facilitate diffusion. However, if the segregation energy is excessively strong, the dislocation core may be pinned with a small number of atoms. The Y and Zn atoms segregate at the Shockley partial dislocation where the segregation energy is enhanced (Fig. 7a and b), nucleating the Y–Zn cluster (top-left panel of Fig. 9). However, the core contains a limited number of available sites. When the cluster size reaches $n \geq 7$, the dislocation moves leftward by expanding the $I_2$-SF (Fig. 8c and 8f and the top-right panel of Fig. 9). Although the cluster structure differs between the segregation in the dislocation core and the $I_2$-SF in bulk, similar changes are expected in their GSFE curves. As shown in Fig. 5, the hcp stacking ($\Delta x/b_{\mathrm{partial}} = 1$) is destabilized and the relative maximum corresponding to

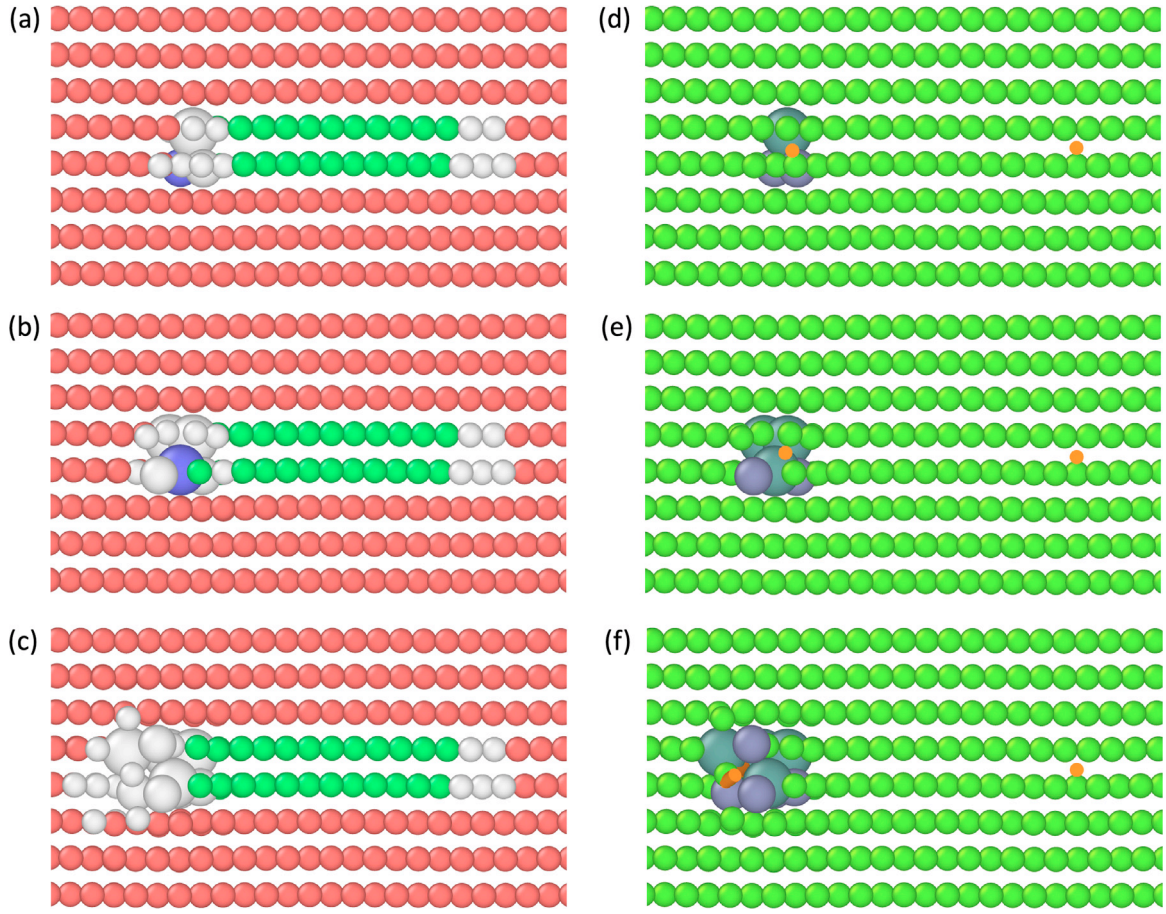


Fig. 8. Segregation behavior at the core of a Shockley partial dislocation for $n = 3$ (a), $n = 6$ (b), and $n = 9$ (c); results of the dislocation extraction algorithm at (d) $n = 3$ (e) $n = 6$ (f), and $n = 9$. Orange line or dots indicate the dislocation line with $1/3\langle\bar{1}010\rangle$. Large (dark green), medium (dark purple), and small (green) dots represent Y, Zn, and Mg atoms, respectively, where the size of Mg atom is reduced for visualization (color online).

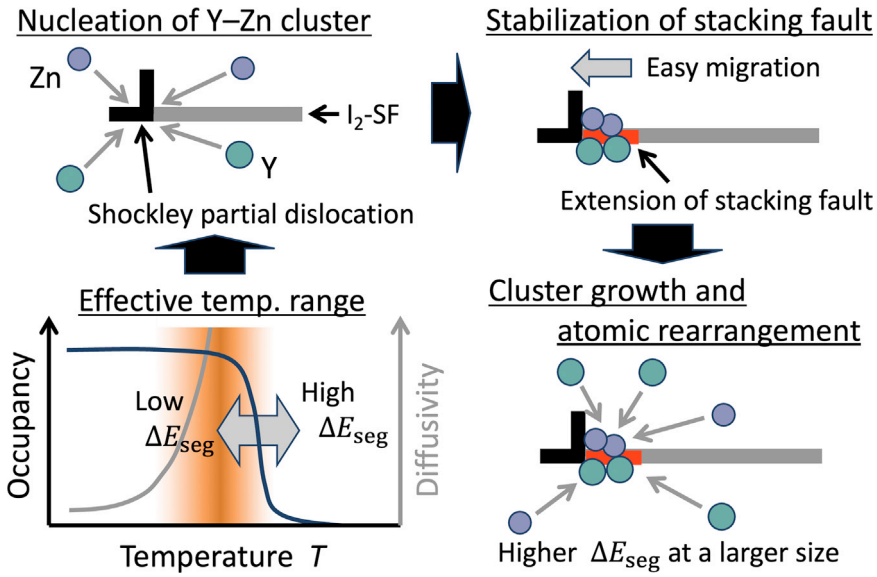


Fig. 9. Schematic of the synchronized growth of Y–Zn cluster and migration of a Shockley partial dislocation (color online).

the unstable SF energy disappears at $n = 7$. This change in the GSFE curve is the likely driving force of the dislocation migration. A cluster of size $n \geq 7$ possesses sufficient segregation energy for the subsequent segregation of Y and Zn atoms (Fig. 7a). Furthermore, the energy requirement of fcc-to-hcp stacking largely increases at $n \geq 8$ (Fig. 6). The following segregation and atom rearrangement is enhanced by the increased vacancy concentration [7], leading to the formation of $LI_2$-type clusters (bottom-right panel of Fig. 9). Repeats of this synchronized behavior, i.e., nucleation of the cluster at the core of the Shockley partial dislocation, destabilization of hcp stacking, and subsequent growth in the SF, eventually forming the CAL. One can reasonably expect that deforming the structure (to create high-density dislocations), moderately increasing the temperature (to enhance the diffusion of Y, Zn, and vacancies without compromising their occupancy), and increasing the solute concentration (to enhance the occupancy) will realize high-density CALs, aspresented in Ref [19]. Furthermore, external stress likely assists the migration of the leading partial dislocation and consequent expansion of the $I_2$-SF, whereas the segregated clusters inhibit migration of the trailing partial dislocation.

The formation mechanism of LPSO phase has been extensively investigated by many researchers, as referred in the introduction [6–8]. In our proposed synchronized mechanisms, the Shockley partial dislocation migrates when its core region becomes enriched with Y and Zn, resulting in the local shear. Additionally, vacancy diffusion is essential for the formation of $L1_2$-clusters. Thus, the proposed mechanism exhibits similarities to certain models for the formation of LPSO phase, including vacancy-mediated cluster formation [7] and the development of Y/Zn enriched regions prior to shear transformation [8]. However, we emphasize that the formation mechanisms of the LPSO-phase and CAL are not necessarily identical. In the case of the LPSO phase, the inter-$I_2$-SF interactions significantly contribute to structural stabilization and the realization of the periodic stacking sequences. In contrast, CAL formation relies solely on intra-plane interactions among segregated atoms to stabilize the $I_2$-SF. While the structural similarities within the $I_2$-SF may suggest some commonality between the formation mechanisms of LPSO phases and CAL, the underlying processes are expected to diverge due to these fundamental differences. Accordingly, the alloy systems that promote CAL formation are also expected differ, to some extent, from those that promote the formation of LPSO phase.

## 4. Conclusion

Herein, we analyzed the cosegregation behaviors of Y and Zn at the $I_2$-SF and the basal edge dislocation in Mg using DFT calculations. We also studied the modification of the GSFE curves accompanying cosegregation at the $I_2$-SF. Our conclusions are summarized below.

(1) Substituting Y and Zn in the $I_2$-SF in a stable order and slightly modifying the atomic positions via vacancy diffusion, we created an $L1_2$-type cluster. The segregation energy of Y or Zn at the nucleation of the cluster is small and the growth rate can be limited by the desorption of the segregated atoms. During the latter stages when the cluster has sufficiently grown ($n \geq 7$), the segregation energy increases and the Y and Zn atoms are captured in the $I_2$-SF.
(2) The Shockley partial dislocation is a strong nucleation site of the Y–Zn cluster. After segregation of several atoms, the hcp stacking is destabilized (or the fcc stacking is stabilized) and the partial dislocation migrates. At this time, the cluster is sufficiently large to maintain its growth in the $I_2$-SF.
(3) The energy requirements of fcc-to-hcp stacking changes greatly increase during the latter half stage of cluster growth. The migration of terminating partial dislocations toward the elimination of the SF are strictly prohibited.
(4) A CAL can be formed through the repeated synchronized behavior of cluster nucleation at the Shockley partial dislocation, dislocation motion (extension of $I_2$-SF), and following of the cluster growth in the $I_2$-SF.

We expect that other CAL-strengthened metallic systems will be found by analyzing the segregation energies of various elements at the Shockley partial dislocation and the SFs and by defining the processing temperature and necessary solute concentrations based on their interaction energies. These materials, which undergo kink strengthening, offer new avenues for the development of Mg-alloys with both high strength and ductility and/or high creep resistance for a range of applications. We also expect that the CAL formation along non-basal planes can be identified using a similar methodology as employed in this paper.

The conventional static framework (i.e., time-independent DFT) exhibits limitations in capturing the kinetics of thermally activated processes in complex phenomena. We anticipate that leveraging time-dependent DFT or state-of-the-art machine learning potentials will enable the elucidation of segregation dynamics with unprecedented spatiotemporal resolution in the near future.

## Funding

This research was supported by the Japan Science and Technology Agency (JST), CREST (grant number JPMJCR2094).

## Data availability

Data will be made available on reasonable request.

## Declaration of competing interest

The authors declare that they have no known competing financial interests on personal relationships that could have appeared to influence the work reported in this paper.

## CRediT authorship contribution statement

**Ryosuke Matsumoto:** Writing – review & editing, Writing – original draft, Visualization, Validation, Supervision, Software, Resources, Project administration, Methodology, Investigation, Funding acquisition, Formal analysis, Data curation, Conceptualization. **Naoki Uemura:** Writing – review & editing, Validation, Methodology, Investigation.

## Acknowledgments

The computation was carried out using the computer resources offered under the category of General Projects by the Research Institute for Information Technology, Kyushu University.

## Appendix

The thin model with 1608 Mg atoms (Fig. A1) was constructed with a small thickness (0.55 nm along the $z$-axis) and a relatively large width and height (10.68 nm and 5.98 nm along the $x$- and $y$-axes, respectively). A vacuum layer (∼2.3 nm) was set above and below the slab. 1 × 1 × 13 k-point meshe was employed for the thin model. As the dislocation core is symmetric, the substitution positions of the first segregation were limited to the left half of the dislocation core (Fig. A1, inset). The substitution positions labeled 1 to 8 and 9 to 17 existed at the tensile and compressive sides of the edge dislocation, respectively.

Table A1 shows the segregation energies of the Zn and Y atoms in the basal dislocation core obtained from the thin model. The segregation energy of the Y atom is larger at the tensile side (positions 1 to 8) and smaller (or negative) at the compressive side (9 to 17). Conversely, the segregation energy of the Zn atom is larger and smaller at the compressive and tensile sides, respectively. Furthermore, the energies of both atoms are maximized and minimized in the core of the Shockley partial dislocation (2, 10, and 11) and its neighboring positions (1, 3, 9, and 12). The absolute value decreases

Table A1
Segregation energies of Zn and Y in the core of a basal edge dislocation in the thin model: Positions ($i = 1 - 17$) are shown in Fig. 1a (inset).

| Tensile side | | | | | | | | | | |
|---|---|---|---|---|---|---|---|---|---|---|
| Position $i$ | | 1 | 2 | 3 | 4 | 5 | 6 | 7 | 8 | |
| $\Delta E^{x_i}_{\mathrm{seg}_1}$ [eV] | Zn | −0.06 | −0.07 | −0.06 | −0.05 | −0.04 | −0.04 | −0.03 | −0.03 | |
| | Y | 0.19 | 0.20 | 0.20 | 0.20 | 0.18 | 0.15 | 0.13 | 0.12 | |
| Compressive side | | | | | | | | | | |
| Position $i$ | | 8 | 10 | 11 | 12 | 13 | 14 | 15 | 16 | 17 |
| $\Delta E^{x_i}_{\mathrm{seg}_1}$ [eV] | Zn | 0.17 | 0.18 | 0.17 | 0.16 | 0.15 | 0.13 | 0.06 | 0.04 | 0.03 |
| | Y | −0.11 | −0.12 | −0.05 | −0.03 | −0.02 | −0.01 | 0.01 | 0.02 | 0.02 |

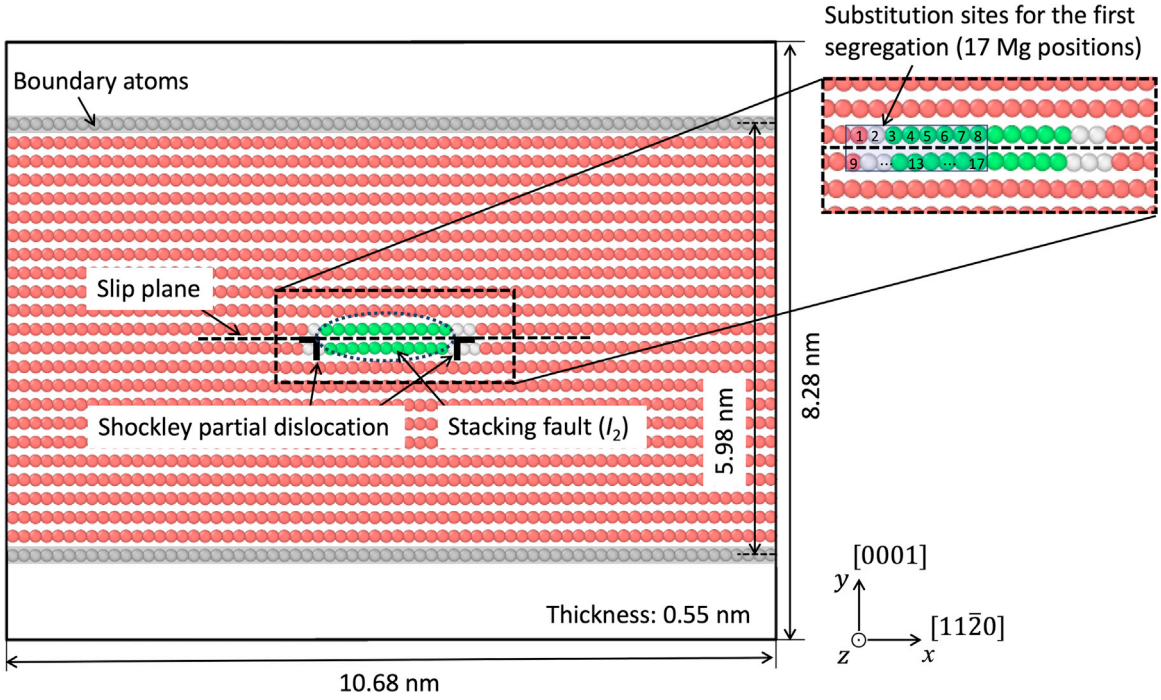


Fig. A1. Atomic structure (thin model) used to analyze the first segregation position of Y and Zn at a basal edge dislocation in Mg. The crystal structures were visualized as described for Fig. 2. Positions 1–8 and positions 9–17 in the inset exist at the tensile and compressive sides of the edge dislocation, respectively. (color online).

as the position moves to the center of the two Shockley partial dislocations (8 and 17). This trend can be explained by the larger and smaller atomic radii of the Y and Zn atoms, respectively, than of the Mg atom (0.180 nm for Y, 0.134 nm for Zn, and 0.160 nm for Mg [42]), allowing natural relaxation of the local tensile and compressive strains, respectively. The dislocation core largely increases the first segregation energies of the Y and Zn atoms to 0.20 and 0.18 eV, respectively, from 0.05 and 0.01 eV, respectively, at $I_2$-SF in the bulk-hcp lattice (Subsection 3.1). Meanwhile, the occupancy of the Y atom increases from 0.05 at $I_2$-SF to 0.65 under the present conditions. The dislocation core clearly functions as the nucleation site of the Y–Zn clusters. At the center position of the two Shockley partial dislocations (8 or 17), the segregation energies of the Y and Zn atoms are 0.12 eV and 0.03 eV, respectively, confirming a non-negligible stress effect in the SF part of the basal dislocation, especially during the initial segregation of the Y atom (additional 0.07 eV to 0.05 eV in $I_2$-SF). The occupancy of the 0.12-eV Y atom ($i = 8$, at the midpoint of the SF part) was obtained as 0.21, indicating that the stress effect quadruples the occupancy during the first segregation. The influence of the stress effect (∼0.07 eV difference in segregation energy) is expected to be small during the later stage of cluster growth ($n \geq 7$), when the segregation energy is relatively large (Table 1) and the occupancy is almost 1 even after modification.

The segregation energy of Y was maximized (∼0.20 eV) at several positions in the tensile side of the dislocation core. Here, we selected position 2 of the Y atom as the first segregation position because it is a Shockley partial dislocation site and corresponds to position 9 or 9′ in the thick model (Fig. 2b and c).

## References


[1] J. She, J. Chen, X. Xiong, Y. Yang, X. Peng, D. Chen, F. Pan, J. Magnes. Alloys. 12 (2024) 3441–3475, doi:10.1016/j.jma.2024.10.001.

[2] Y. Kawamura, K. Hayashi, A. Inoue, T. Masumoto, Mater. Trans. 42 (2001) 1172–1176, doi:10.2320/matertrans.42.1172.

[3] E. Abe, A. Ono, T. Itoi, M. Yamasaki, Y. Kawamuwa, Philos. Mag. Lett. 91 (2011) 690–696, doi:10.1080/09500839.2011.609149.

[4] D. Egusa, E. Abe, Acta Mater. 60 (2012) 166–178, doi:10.1016/j.actamat.2011.09.030.

[5] K. Kishida, H. Yokobayashi, H. Inui, M. Yamasaki, Y. Kawamura, Intermetallics 31 (2012) 55–64, doi:10.1016/j.intermet.2012.06.010.

[6] H. Kimizuka, S. Kurokawa, A. Yamaguchi, A. Sakai, S. Ogata, Sci. Rep. 4 (2014) 7318, doi:10.1038/srep07318.

[7] M. Itakura, M. Yamaguchi, D. Egusa, E. Abe, Acta Mater. 203 (2021) 116491, doi:10.1016/j.actamat.2020.116491.

[8] J.K. Kim, L. Jin, S. Sandlöbes, D. Raabe, Sci. Rep. 7 (2017) 4046, doi:10.1038/s41598-017-04343-y.

[9] M. Yamasaki, K. Hashimoto, K. Hagihara, Y. Kawamura, Acta Mater. 59 (2011) 3646–3658, doi:10.1016/j.actamat.2011.02.038.

[10] J. Zhou, X. Luo, H. Yang, B. Jiang, W. Xie, Z. Dong, J. Song, J. Xu, G. Huang, D. Zhang, F. Pan, J. Mater. Res. Technol. 24 (2023) 7258–7269, doi:10.1016/j.jmrt.2023.04.252.

[11] X. Wang, Y. Zhao, M. Li, S.X. Tang, Y. Huang, Y. Liu, C. Huang, Mater. Sci. Eng. A. 917 (2024) 147411, doi:10.1016/j.msea.2024.147411.

[12] S. Nishimoto, T. Yasuda, K. Hagihara, M. Yamasaki, J. Magnes. Alloys. 12 (2024) 2952–2966, doi:10.1016/j.jma.2024.07.018.

[13] S. Harjo, W. Gong, K. Aizawa, T. Kawasaki, M. Yamasaki, Acta Mater. 225 (2023) 119029, doi:10.1016/j.actamat.2023.119029.

[14] Y. Kawamura, M. Yamasaki, Mater. Trans. 48 (2007) 2986–2992, doi:10.2320/matertrans.MER2007142.

[15] S. Ishizaki, M. Yamasaki, K. Hagihara, S. Nishimoto, T. Nakamura, Y. Kawamura, Mater. Trans. 64 (2023) 756–765, doi:10.2320/matertrans.MT-MD2022015.

[16] K. Hagihara, R. Ueyama, M. Yamasaki, Y. Kawamura, T. Nakano, Acta Mater 209 (2021) 116797, doi:10.1016/j.actamat.2021.116797.

[17] K. Hagihara, R. Ueyama, T. Tokunaga, M. Yamasaki, Y. Kawamura, T. Nakano, Mater. Res. Lett. 9 (2021) 467–474, doi:10.1080/21663831.2021.1974593.

[18] C. He, Y. Zhang, Z. Li, H. Chen, J.F. Nie, J. Magnes. Alloys. 12 (2024) 3135–3141, doi:10.1016/j.jma.2022.11.021.

[19] T. Mineta, D. Takahashi, W. Bando, H. Sato, K. Hagihara, M. Yamasaki, Mater. Today Commun. 39 (2024) 108912, doi:10.1016/j.mtcomm.2024.108912.

[20] R. Matsumoto, Eng. Frac. Mech. 306 (2024) 110250, doi:10.1016/j.engfracmech.2024.110250.

[21] R. Matsumoto, S.T. Oyinbo, M. Vijendran, S. Taketomi, ISIJ Int. 62 (2022) 2402–2409, doi:10.2355/isijinternational.ISIJINT-2022-311.

[22] G. Kresse, J. Furthmüller, Phys. Rev. B. 54 (1996) 11169–11186, doi:10.1103/PhysRevB.54.11169.

[23] J.P. Perdew, K. Burke, M. Ernzerhof, Phys. Rev. Lett. 77 (1996) 3865–3868, doi:10.1103/PhysRevLett.77.3865.

[24] P.E. Blöchl, Phys. Rev. B 50 (1994) 17953–17979, doi:10.1103/PhysRevB.50.17953.

[25] H.J. Monkhorst, J.D. Pack, Phys. Rev. B 13 (1976) 5188–5192, doi:10.1103/PhysRevB.13.5188.

[26] N. Uemura, S. Singhaneka, R. Matsumoto, Mater. Trans. 65 (2024) 1080–1088, doi:10.2320/matertrans.MT-M2024056.

[27] S. Singhaneka, R. Matsumoto, Comp. Mater. Sci. 230 (2023) 112458, doi:10.1016/j.commatsci.2023.112458.

[28] J.P. Hirth, J. Lothe, in: Theory of dislocations, second ed., Krieger Publishing Company, Malabar, FL, 1982, p. 368.

[29] M. Vijendran, R. Matsumoto, Sci. Technol. Adv. Mater. 26 (2025) 2459060, doi:10.1080/14686996.2025.2459060.

[30] D. McLean, Grain boundaries in metals, Oxford University Press, London, 1957.

[31] S. Taketomi, R. Matsumoto, N. Miyazaki, Acta Mater 56 (2008) 3761–3769, doi:10.1016/j.actamat.2008.04.011.

[32] R. Matsumoto, Scr. Mater. 249 (2024) 116152, doi:10.1016/j.scriptamat.2024.116152.

[33] R. Matsumoto, S.T. Oyinbo, D. Matsunaka, Sci. Mater. 252 (2024) 116235, doi:10.1016/j.scriptamat.2024.116235.

[34] J.D. Honeycutt, H.C. Andemen, J. Phys. Chem. 91 (1987) 4950–4963, doi:10.1021/j100303a014.

[35] A. Stukowski, Model. Simul. Mater. Sci. Eng. 18 (2010) 015012, doi:10.1088/0965-0393/18/1/015012.

[36] L.J. Zhang, T.I. Spiridonova, S.E. Kulkova, R. Yang, Q.M. Hu, Comp. Mater. Sci. 128 (2017) 236–242, doi:10.1016/j.commatsci.2016.11.033.

[37] S. Ganeshan, L.G. Hector, Z.K. Liu, Comp. Mater. Sci. 50 (2010) 301–307, doi:10.1016/j.commatsci.2010.08.019.

[38] B.C. Zhou, S.L. Shang, Y. Wang, Z.K. Liu, Acta Mater. 103 (2016) 573–586, doi:10.1016/j.actamat.2015.10.010.

[39] T. Tsuru, Y. Udagawa, M. Yamaguchi, M. Itakura, H. Kaburaki, Y. Kaji, J. Phys. Condens. Matter. 25 (2013) 022202, doi:10.1088/0953-8984/25/2/022202.

[40] Q. Dong, Z. Luo, H. Zhu, L. Wang, T. Ying, Z. Jin, D. Li, W. Ding, X. Zeng, J. Mater. Sci. Technol. 34 (2018) 1773–1780, doi:10.1016/j.jmst.2018.02.009.

[41] A. Stukowski, K. Albe, Model. Simul. Mater. Sci. Eng. 18 (2010) 085001, doi:10.1088/0965-0393/18/8/085001.

[42] J.A. Dean, Lange's handbook of chemistry, 15th ed., McGraw-Hill, New York, 1999.